RSC Advances

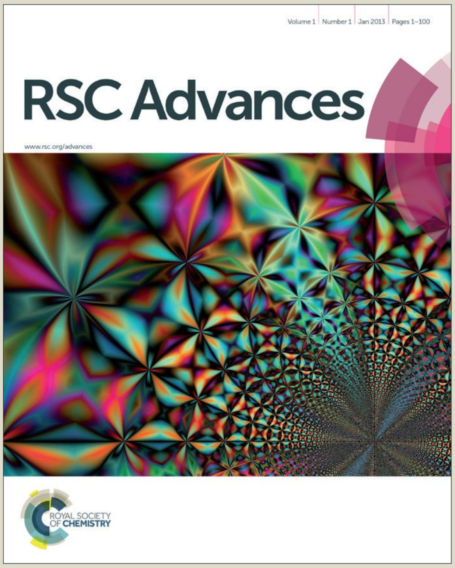

ROYAL SOCIETY OF CHEMISTRY

www.rsc.org/advances

Synthesis and characterization of ZnO nanorods with narrow size distribution

Chandrakanth Reddy Chandraiahgari,[*,||,‡] Giovanni De Bellis,[||,‡] Paolo Ballirano,[§,||], Santosh Kiran Balijepalli,[ꟷ] Saulius Kaciulis,[ꟷ] Luisa Caneve,[#] Francesca Sarto,[#] and Maria Sabrina Sarto.[*,||,‡]*

‡ Department of Astronautics, Electrical and Energetics Engineering, Sapienza University of Rome, via Eudossiana 18, Rome 00184, Italy

§ Department of Earth Sciences, Sapienza University of Rome, Piazzale Aldo Moro 5, Rome 00185, Italy

|| Research Center on Nanotechnology Applied to Engineering of Sapienza (CNIS), SNNLab, Sapienza University of Rome, Piazzale Aldo Moro, 5, Rome 00185, Italy

[ꟷ] CNR - ISMN, P.O. Box 10, 00015 Monterotondo Stazione, Rome, Italy

[#] ENEA, Centro Ricerche Frascati, Via Enrico Fermi 45, Frascati 00044, Italy

Corresponding Authors:

* E-mail: c.chandraiahgari@uniroma1.it; mariasabrina.sarto@uniroma1.it

Keywords: Zinc Oxide nanorods, thermal decomposition method, size distribution, XRD, XPS, PL

Abstract

The development of novel materials for energy harvesting applications or strain sensing has determined a great interest towards zinc oxide (ZnO) nanostructures, and in particular towards the synthesis of ZnO nanowires or nanorods with well controlled morphology and properties. The high-yield mass production of such nanostructures through catalyst-free methods is a crucial aspect to enable a cost-effective large-scale development of new ZnO-based piezoelectric devices and materials. In the present work, we propose a method for the mass-production of high-purity ZnO-nanorods with uniform size distribution, based on the combination of thermal decomposition of zinc acetate dihydrate and probe sonication in acetone. The quality of the produced ZnO nanorods is assessed through multi-technique characterization using field-emission scanning electron microscopy (FE-SEM), X-ray diffraction (XRD), transmission electron microscopy (TEM), X-ray photoelectron spectroscopy (XPS), and photo-luminescence spectroscopy (PL). The adopted synthesis method is simple, cost effective and feasible for large-scale production. Various process parameters such as precursor amount and growth time have been found to play an important role in controlling the formation of the as grown nanostructures with high uniformity in size and morphology. Size distribution curves are employed to depict the effect of various process parameters for tailoring the morphology, homogeneity and aspect ratio of the nanorods. Our results reveal that the high crystallographic quality of ZnO nanorods grown by long-time thermal decomposition method is not affected by probe sonication, which is proposed as a post-synthesis step necessary to produce ZnO nanorods powder with a uniform distribution of diameters and lengths.

Introduction

Zinc oxide (ZnO) is one of the significant technological materials due to its remarkable performance in a wide range of multi disciplinary fields such as nanoscale optoelectronics, self-powered micro-/nano systems, and nanomedicine.[1-3] It is a wide-band gap semiconducting material with a direct gap of 3.37 eV and a relatively large exciton binding energy of 60 meV at room temperature.[4] It crystallizes preferentially in the hexagonal wurtzite-type structure and forms a variety of nanostructures.[5] Such nanostructures exhibit unique optical, electronic, physical and chemical properties owing to their size and morphology. Being a biosafe and biocompatible material and abundantly available low cost fabrication techniques, it finds a wide range of existing or emerging commercial applications, including transparent UV shielding films, transparent conducting oxides, UV photo detectors, light-emitting diodes, solar cells, gas sensors, bio sensors, cosmetics, food products preservation, and nanoantibiotics.[6-11]

The rise in demand for large-scale amount of engineered ZnO nanomaterials in diverse commercial products is due to their UV light absorption, semi-conducting, catalytic, and antibacterial properties. The enormous interest in ZnO is due to their unique ability of possessing structural dependent characteristics. It has been reported that the physical, chemical and optical properties of the nanostructures such as piezoelectricity, antimicrobial activity, photocatalytic activity and photoluminescence are strongly dependent on ZnO structure size, shape and morphology.[12-17]

Main efforts have been devoted to the synthesis of aligned arrays of ZnO nanorods (NRs) or nanowires (NWs).[10] Vapor-liquid-solid synthesis (VLS) has been extensively explored in the literature as an approach to the formation of one-dimensional (1D) ZnO nanostructures such as whiskers, nanorods and nanowires.[18-23] Synthesis of ZnO nanorods via chemical approaches is an alternative to the aforementioned methods, opening the route to low-cost catalyst-free mass-production of ZnO nanostructures.[24-28]

In the last years, there has been an escalation in the development of various techniques for large-scale synthesis of ZnO-NRs or NWs. Recently, vapor phase thermal decomposition method (TDM)[27,28] and solution phase hydrothermal method (HTM)[31-32] have emerged as promising techniques for the synthesis of ZnO nanostructures, as they are simple, catalyst-free and inexpensive. They involve relatively few reaction steps, without use or production of volatile and toxic substances, and they are suitable for large-scale production. However, the main difficulty of such techniques when applied for mass-production purposes consists in the selective control of the morphology of the grown nanostructures through the proper setting of the process parameters, in order to obtain the desired shape and dimensions, with minimum dispersion in diameter size and single-mode distribution of lengths. In a previous study[30], it has been reported that the aspect ratio and density of ZnO nanostructures synthesized by TDM can be controlled through the proper setting of growth temperature and duration. However, high-purity ZnO-NRs can be produced only with synthesis time longer than several hours, as it was demonstrated by PL analysis.[29] The effect of precursor amount on the homogeneity and crystalline quality of the produced ZnO-NRs produced by TDM has not been extensively investigated yet. Similarly, it is known that precursor concentrations, growth temperature and duration have an influence on the morphology and aspect ratio of the nanostructures synthesized by HTM.[32-34] However, it is observed that in general TDM, compared to HTM, enables the synthesis of ZnO-NRs or NWs with a higher aspect ratio (defined as the ratio between length and diameter of an 1D structure) and better uniformity of diameter size and length along the axis. Therefore, it is of paramount importance the development and understanding of the process parameters for large-scale synthesis of ZnO nanostructures, enabling a good control over morphology and a narrow size distribution.

In this work, we investigate the catalyst-free production route of ZnO nanorods with uniform size distribution and high purity, through the combination of thermal decomposition of zinc acetate dihydrate and a post-synthesis step of probe sonication in acetone. The scope of this paper is to develop a synthesis route of ZnO-NRs with uniform size distribution (in terms of diameter and length) and high purity, suitable for scaling up in mass-production applications, like piezoresistive or piezoelectric nanocomposites. Actually, the TDM as presented in the literature[29] leads to the production of ZnO-NRs with a wide distribution of lengths, ranging from a few hundred of nanometers up to several microns.

In order to define the growth conditions suitable for mass production of ZnO-NR powder, we investigate the effects of both precursor amount and growth period on the synthesis process. A multifunctional characterization of the produced nanomaterials is performed through field emission scanning electron microscopy (FE-SEM), X-ray diffraction (XRD), transmission electron microscopy (TEM), X-ray photoelectron spectroscopy (XPS), and photo-luminescence spectroscopy (PL), in order to demonstrate the superior crystallographic properties of ZnO nanorods, treated or not by probe sonication, with respect to other types of ZnO structures, like microrods (MRs) and nanoparticles (NPs) synthesized by hydrothermal method as described in the Supporting Information. We show that probe sonication affects only the morphology of ZnO-NRs and can be used to obtain high-purity powders with narrow distribution of diameters (~36 nm ± 10 nm) and single-mode distribution of lengths (~470 nm ± 330 nm).

Experimental

ZnO-NRs with uniform size distribution were produced starting from zinc acetate precursor, through the five-step process sketched in Figure 1 and described in the following.

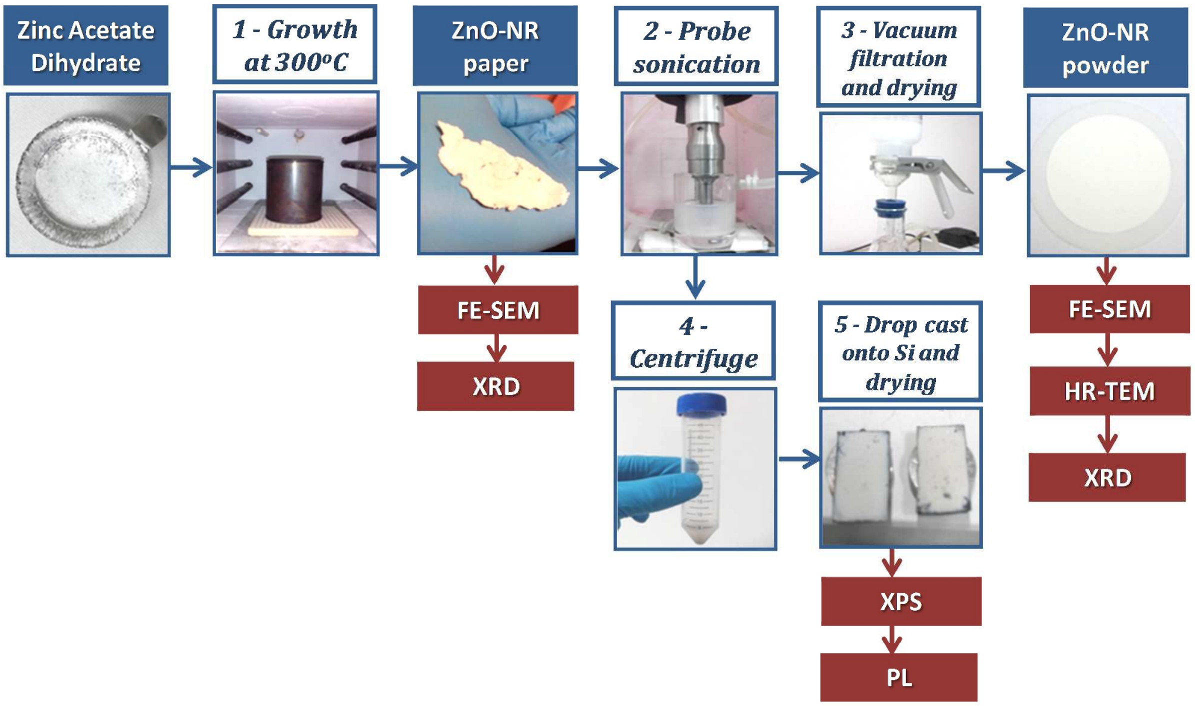

Figure 1. Schematic of the ZnO-NRs production route and characterization process.

Materials

All chemicals were of reagent grade and used as received without further purification: Zinc acetate dihydrate ($Zn(CH_3COO)_2{\cdot}2H_2O$, Sigma-Aldrich, ACS reagent, ≥ 98%) and Acetone ($(CH_3)COCH_3$, Fisher Chemical, ACS reagent, ≥ 99%).

Synthesis of ZnO Nanorods

ZnO-NRs were synthesized through the thermal decomposition method according to the procedure described by Chih-Cheng Lin et al.[27] In the typical synthesis process, a specific amount of zinc acetate dihydrate was distributed uniformly inside a disposable aluminum foil dish (TAAB, UK, 53 mm Diam. x 17 mm deep) with area of 22 cm^2, closely packed with an aluminum foil, and finally placed inside a tightly closed steel box. The steel box was subsequently placed inside a preheated laboratory muffle furnace (Lenton UAF 15/10) at 300°C in air for 12 h, producing porous papers of ZnO-NRs. Zinc acetate dihydrate served as precursor for the synthesis and we did not use any other catalysts. The influence of precursor amount was evaluated using three different quantities, namely 0.1 g, 0.3 g and 0.5 g, while maintaining the growth time for 12 h. The influence of short growth time of 3 h and 6 h was also evaluated for the precursor amount of 0.3 g.

ZnO-NR suspensions were produced by dispersion of the ZnO-NR paper in Acetone, with concentration of 1 mg/ml, through a probe sonication, using a Sonics &Materials Vibracell VCX750. During the sonication, the suspensions were maintained at a constant temperature of 15°C through a jacketed beaker, using a water bath circulator. After the sonication, ZnO-NR powders were recollected upon vacuum filtration with an alumina membrane (having pore size of 20~nm) and underwent drying in oven at 120°C for 15 min to remove any residual solvent. We performed two different sonication cycles:

i) A short sonication (SS) in pulse mode (1-sec on-phase and 1-sec off-phase) for 5 min, with ultrasound amplitude set at 40%, having the scope of uniformly dispersing ZnO-NRs, without altering their initial diameter and length, thus obtaining ZnO-NR powders with dual mode distribution of lengths as shown in the section “Results”;

ii) A long sonication (LS) in pulse mode (1-sec on-phase and 1-sec off-phase) for 20 min, with ultrasound amplitude set at 70%, having the scope of chopping the longest nanowires in order to produce, after filtration, ZnO-NRs powder (NRL) characterized by a single-mode distribution of length.

Characterizations

The morphology of the ZnO nanostructures was observed using a field emission scanning electron microscope (FE-SEM, Zeiss Auriga), available at SNN-Lab, at different steps of the production process, as sketched in Fig.1. Samples for FE-SEM analysis were prepared by placing a small specimen of ZnO-NRs paper or a small amount of ZnO-NRs powder over an adhesive conductive copper tape. The papers were observed on both top and bottom faces and at fracture borders.

Numerically extrapolated probability distribution function (PDF) and empirical cumulative distribution function (CDF) curves were employed for the graphical representation of the size distribution of the ZnO-NRs (i.e. length and diameter), as per FE-SEM observations. To this purpose, a minimum of 50 measurements of each physical dimension were recorded from FE-SEM images.

The structural characterization and phase identification of the synthesized ZnO-NRs were performed by X-ray diffraction using a Bruker AXS D8-Advance diffractometer, operating in θ-θ transmission geometry, equipped with focusing Göbel mirrors along the incident beam, Soller slits on both incident and (radial) diffracted beams, and a PSD VANTEC-1 detector. Samples were prepared by loading the powders into 0.3 mm diameter borosilicate capillaries that were aligned onto a standard goniometer head. XRD data were collected at room temperature (RT), using Cu Kα radiation (λ =1.5418Å, 40 kV at 40 mA), in a 2θ angular range spanning from 20° to 145° with a step size of 0.022° and 1 s of counting time. Structural refinements were performed by the Rietveld method using TOPAS v.4.2 (Bruker AXS 2009) software.

Peak shape was modelled through the Fundamental Parameters Approach (FPA), imposing the following full axial parameters: divergence slit: 0.3°, source length 12 mm, sample length and receiving slit length 12.7 mm. The starting structural parameters of zincite were taken from Sowa and Ahsbahs.[35] Absorption was modelled following the Sabine model for cylindrical samples[36] and the background was fitted by a Chebychev polynomial of the first kind. The occurrence of preferred orientation was tested by means of spherical harmonics (eight refinable parameters up to the 8th order). The selection of the number of terms to be used was performed following the procedure devised by Ballirano.[37] A marginal improvement of the fit was observed as a result of the nearly absence of texture, which is typical of a capillary mount. According to the shape of the crystallites, refinements were performed using the recently proposed ellipsoid-model of Katerinopoulou et al.[38] describing the diffraction-vector dependent broadening of diffraction maxima. In the hexagonal symmetry, the shape ellipsoid parameters b_{ij} are constrained as $b_{11} = b_{22} = 2b_{12}; b_{13} = b_{23} = 0$. The ellipsoid is oriented with the principal radii $r_a \perp c$ and $r_c \,||\, c$.

Crystallinity of the nanostructures was probed by using transmission electron microscopy (TEM) using a FEI Tecnai F20 ST TEM operated at beam energy of 200 keV. The samples for TEM were prepared by drop casting the ZnO-NR suspensions (produced either by SS or LS) onto lacey carbon coated 200 mesh Cu grids, with subsequent drying in air.

Samples for XPS and PL analyses were prepared from ZnO-NR suspensions (produced either by SS or LS). Concentrated solution of ZnO-NR suspension obtained upon centrifugation (at 193 g for 10 min) was drop-casted onto a cleaned silicon substrate, with subsequent drying in air.

Chemical composition and purity analysis was performed by X-ray Photoelectron Spectroscopy (XPS) and Auger Electron Spectroscopy (AES) using a monochromatized spectrometer Escalab 250Xi (Thermo Fisher Scientific, UK) equipped with six-channeltron detection system for spectroscopy. The measurements were performed on ZnO samples deposited on silicon substrates and placed inside an ultra-high vacuum (UHV) chamber, using the X-ray source set to the diameter of 900 µm, the analyser at constant pass energy of 20 eV and standard mode of electromagnetic input lenses. Photoelectrons were excited by using a standard Al Kα excitation source, whereas spectroscopic data were processed by the Avantage v.5 software (Thermo Fisher Scientific, UK). In the quantification procedure was included the dependence of photoemission signal intensity on kinetic energy of photoelectrons from different core levels.

The optical properties and crystal defects of the ZnO nanostructures were studied through room temperature photoluminescence (PL) using an excitation source the 266 nm line of a Nd:YAG pulsed laser (Thomson DIVA), with 10 ns pulse length and 20 Hz repetition rate. Crystalline silicon has been chosen as support of the ZnO nanostructures, because it was verified to not produce any PL signal under the considered laser excitation conditions. Energy dispersion of the PL signal was obtained by using a 3648-element linear silicon CCD array, operating in the 200 - 1100 nm wavelength range. The PL spectra were repeated on each sample at three different levels of the laser mean power (i.e. 700, 900 and 1300 ± 100 W/m^2), to investigate the possibly different behavior of defect-related and intrinsic PL signals. Each spectrum was repeated for 16 times on the same sample and subtracted from the background acquired by blocking the laser source. The average values are reported versus the emission energy in Fig. 9. Standard deviation of PL peak values ranged from 4% to 15%, depending on the PL intensity; the data in the interval of 525 - 540 nm were omitted to filter out the strong reflection signal at 532 nm by the 2nd harmonic of the incident laser source.

FE-SEM imaging and XRD were also performed on the ZnO-NRs produced either by SS or LS, after vacuum filtration of the suspensions, and drying of the so-obtained residual material in oven at 120°C for 15 min, to remove any residual solvent.

Results

ZnO-NRs were synthesized through a TDM. FE-SEM analysis revealed that the as-grown NRs are arranged in the form of a porous paper as shown in the SI (Fig.S2), characterized by a well different morphology of the ZnO-NRs grown either on the top or bottom side or across the section. Synthesis of the nanostructures was carried out using the precursor zinc acetate dihydrate at three different amounts (by weight), namely 0.1 g, 0.3 g, and 0.5 g, while maintaining the fixed growth time of 12 h in a muffle furnace at 300°C, and with an amount of precursor of 0.3 g considering increasing growth times of 3 h, 6 h and 12 h at the constant temperature of 300°C. The produced ZnO-papers are reported in Table 1. The production yield obtained ranges between 30% and 34%, which is close to its theoretical yield of 37% [29]. The total amount of produced ZnO-NRs increases proportionally to the precursor amount.

Table 1. ZnO-NR papers produced under different experimental conditions (precursor amount and growth time): measured weight and production yield.

ZnO-paper	Zinc acetate dihydrate (g)	Growth time (h)	Weight (mg)	Yield rate(wt.%)
P1	0.1	12	34.2	34.2
P2	0.3	12	90.3	30.1
P3	0.5	12	157.3	31.4
P4*	0.3	3	96.9	32.3
P5	0.3	6	91.7	30.6

* Due to the short synthesis time the P4 assumes the form of a sponge-like porous material as shown in the SI.

The fracture section of ZnO-NR papers produced with different precursor amount of 0.1 g and 0.3 g are observed through FE-SEM are shown in the SI (Fig. S1A and S1B, respectively). It can be noted that NRs having length longer than a few microns can be observed only on the top side of the paper obtained using 0.3 g of precursor (Fig. S1B).

It results that the morphology (i.e. diameter and length) of the ZnO-NRs grown on the bottom side of the paper is well different from the one of the nanostructures grown on the top side, as shown in Figures 2 A-F. In particular, for increasing amount of precursor (i.e. from 0.1 g to 0.5 g), the difference in length and diameter of the ZnO-NRs observed on the top and bottom sides of the paper also increases. Papers produced with 0.1 g of precursor, consist of ZnO-NRs with diameter below 100 nm on both sides. Nevertheless on the top face there are NRs with length up to a micron (Fig. 2A), whereas the ZnO nanostructures observed on the bottom have a length limited to a few hundreds of nanometers (Fig. 2B). In case of 0.3 g precursor, the papers are made of longer ZnO-NRs on the top face (Fig. 2C) than on the bottom one (Fig. 2D), where the average lengths of the ZnO nanostructures is limited to a few hundreds of nanometers, and we also observed the formation of some clusters of very short NRs. Finally, the papers produced with 0.5 g of precursor are characterized on the top side by a uniform distribution of NRs, with a diameter in the range of 20 - 40 nm (Fig. 2F). On the contrary, the bottom side of such papers consists of ZnO rods with a diameter ranging from 20 - 30 nm (i.e. NRs) up to a few hundreds of nanometers (e.g. MRs) (Fig. 2G).

We also investigated the effect of the growth time on the morphology of the ZnO-NRs on the top face of the paper produced with 0.3 g of precursor. We noticed that after only 3 h, the produced porous material assumes the form of a sponge, composed of ZnO-NRs with an average length of

~390 nm. In that case, we did not observe an organized stratification of the porous material, with relevant morphological differences between ZnO-NRs grown in different positions. After 6 h of growth time, we observed the formation of a paper-like porous paper, with a stratification of ZnO-NRs assuming different morphology on the top and bottom faces: in particular, the NRs grown on the top side of the porous paper (Fig. 2G) have a very similar morphology with respect to the ones grown after 12 h (Fig. 2C).

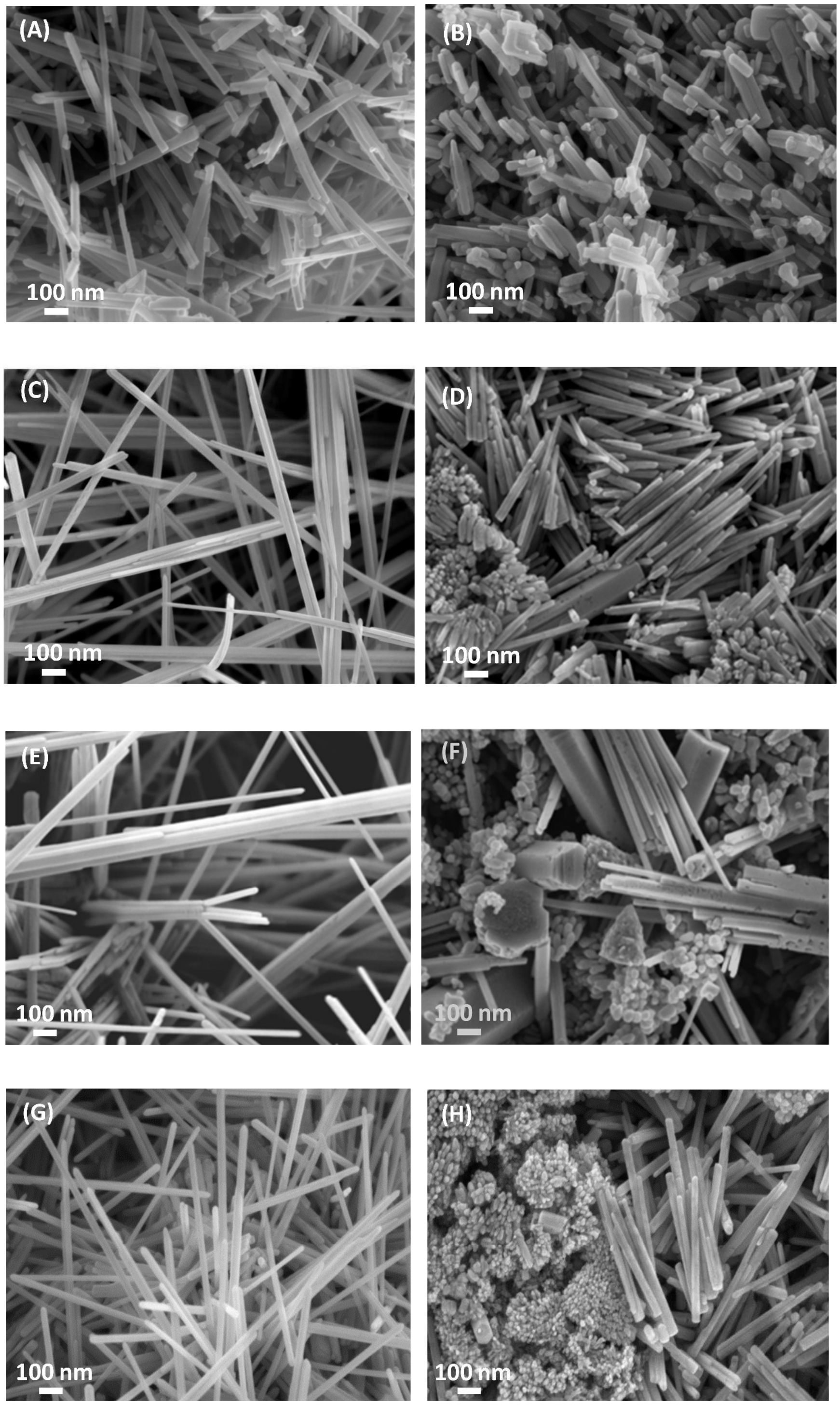

Figure 2. FE-SEM images of ZnO-NRs on the top (A, C, E, G) and bottom (B, D, F, H) faces of the porous paper grown under different conditions: 0.1 g of precursor and 12 h at 300°C (A,B); 0.3 g of precursor and 12 h at 300°C (C,D); 0.5 g of precursor and 12 h at 300°C (E,F); 0.3 g of precursor and 6 h (G,H) at 300°C.

Table 2 summarizes the estimated mean values and standard deviations of diameter and length of ZnO-NRs observed on the top and bottom faces of the produced papers, as they result from FE-SEM analyses. It can be observed that the ZnO-NR diameter gets larger as the precursor amount increases, setting the growth time at 12 h. Higher values of standard deviation are representative of a larger presence of aggregates. In this study, the synthesis of ZnO-NRs using 0.3 g of precursor amount is considered as an optimum choice in the range 0.1-0.5 g, because it represents the best compromise to have NR average diameter below 50 nm and length up to few microns.

The growth of ZnO NRs is understood further by the experiments carried out with a shorter reaction growth time, i.e. only for 3 and 6 h with a precursor amount of 0.3 g. For the growth time of 3 h, we noticed that the average length of the grown NRs is limited to ~390 nm, whereas after 6 h it reaches ~790 nm. Moreover, a previous study has demonstrated that ZnO-NRs grown by TDM improve their photoluminescence properties with increasing growth time.[29] Therefore, in the following we focus our study only on ZnO-NRs produced from the paper P2.

Table 2. Mean values and standard deviations (in brackets) of diameter and length of ZnO-NRs on the top or bottom sides (indicated as NRxT and NRxB respectively) of the papers listed in Table 1, or obtained by LS of the paper P2 (indicated as NRxL).

ZnO-NR	ZnO-paper	Sonication	Diameter (nm)	Length (μm)
NR1T	P1	No	36 (11)	0.43 (0.17)
NR1B	P1	No	45 (18)	0.17 (0.10)
NR2T	P2	No	36 (10)	2.67 (0.58)
NR2B	P2	No	46 (24)	0.17 (0.10)
NR3T	P3	No	39 (15)	2.67 (1.11)
NR3B	P3	No	65 (39)	1.39 (0.40)
NR4T	P4	No	35 (10)	0.39 (0.23)
NR5T	P5	No	35 (11)	0.79 (0.38)
NR5B	P5	No	33 (12)	0.20 (0.13)
NR2L	P2	LS	36 (10)	0.47 (0.33)

ZnO-NRs are obtained by probe sonication of the produced papers in acetone. We observed through FE-SEM imaging that a SS does not affect remarkably length and diameter of the ZnO-NRs (Figs. 3A and B). On the contrary, a more homogeneous size distribution of ZnO-NRs was obtained after LS of the P2 paper, as reported in Table 2. We noticed that ZnO-NRs were chopped during LS, but their diameter was not affected, as shown in Figs. 3C and D. A similar effect was noticed also on ZnO-MRs, as reported in the SI.

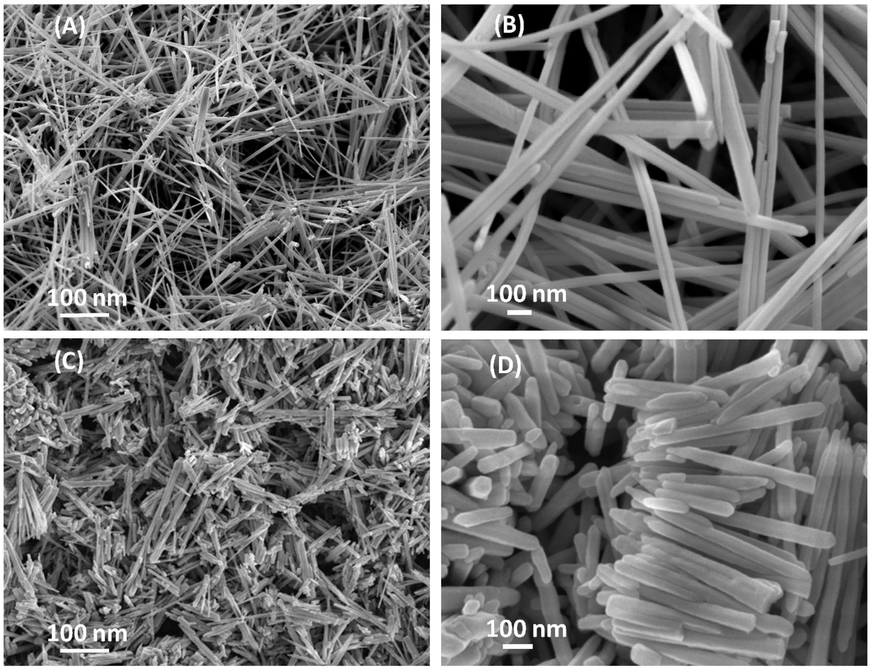

Figure 3. FE-SEM images of ZnO-NRs produced through SS (A, B) or LS (C, D) in acetone of the porous paper grown for 12 h at 300°C using 0.3 g of precursor.

The cumulative distribution function (CDF) of lengths for the different types of ZnO-NRs produced using 0.3 g of precursor (Table 2) was calculated and reported in Fig. 4A. We noticed that for increasing growth time, the dispersion between the CDFs at 50% associated to NRs on the top and bottom sides of the same paper raises up (from ~0.6 μm for 6 h growth time to ~2.5 μm for 12 h growth time). The 50% CDF for ZnO-NRs produced by LS of the paper P2 corresponds to the length of 0.47 μm. The diameter CDF of the ZnO-NRs produced by LS of the paper P2 is reported in Fig. 4B: it is confirmed that the LS does not affect remarkably the nanorods diameter.

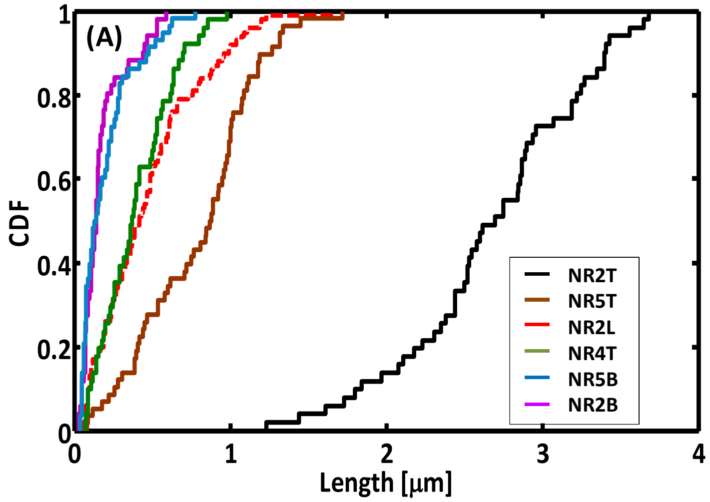

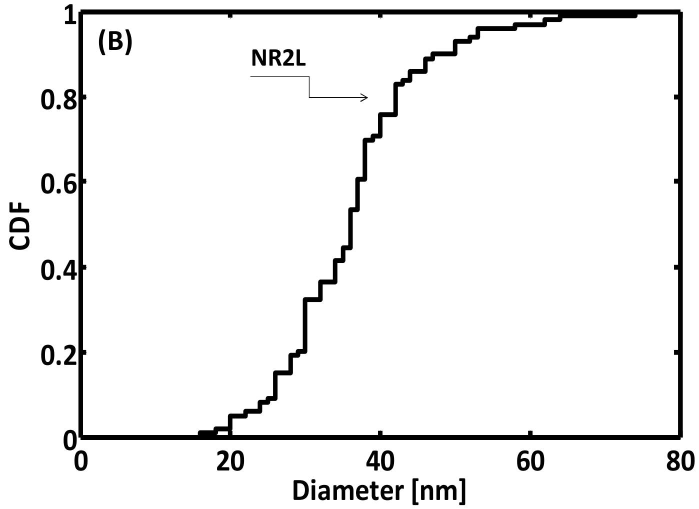

Figure 4. Length CDF of ZnO-NRs produced with 0.3 g of precursor (A) and diameter CDF of the NRs obtained by LS of the paper P2 (B).

Therefore, we assumed that LS can be used for the production of ZnO-NRs with single-mode length distribution. In order to validate such assumption, we investigated the structural and optical properties of the produced nanostructures, as described in the following.

The crystalline structure of the ZnO-NRs powders, produced by SS and LS of the paper P2 in acetone, was evaluated by XRD analysis. Figure 5 shows the recorded diffraction patterns of the synthesized ZnO-NRs produced by LS (NR2L) or by SS (NR2S), compared with the ones of ZnO-MRs (MR) and of ZnO-NPs (NP) synthesized as described in the SI. The sharp and intense peaks of the spectra in Fig. 5 demonstrate the highly crystalline nature of the synthesized ZnO structures. Moreover, all four diffraction patterns are in good agreement with the one published in Joint Committee on Powder Diffraction Standards (JCPDS) card 036-1451 for hexagonal wurtzite structure of ZnO.

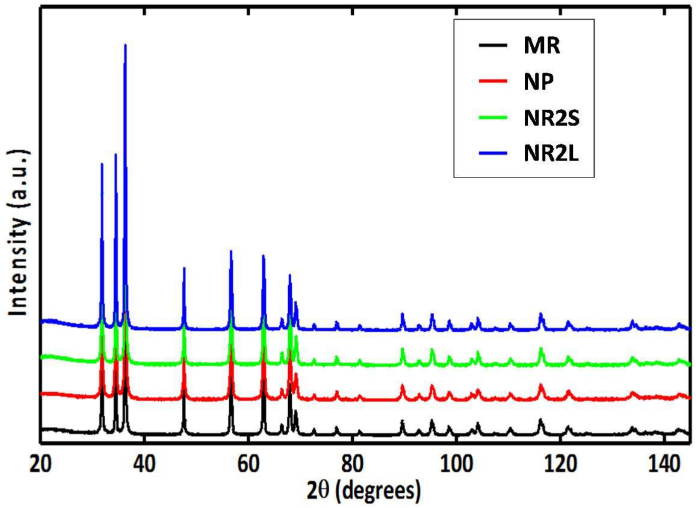

Figure 5. X-ray diffraction patterns of ZnO-NRs produced from paper P2 by SS and LS, and of ZnO-MRs and ZnO-NPs synthetized as described in the SI.

A careful scrutiny of the diffraction patterns in Fig. 5 confirmed the absence of any detectable crystalline impurity, within the limits of the diffractometer sensitivity, which is estimated to be of ca. 0.1 wt%.

Structural information of the analyzed micro- and nano-structures is reported in Table 3. Zincite has the hexagonal ZnS wurtzite structure, and it is characterized by cell parameters and volume of the reference sample that are smaller than those of all micro- and nano-structures investigated in this study, in agreement with previous findings on other simple oxides.[39-41] All analyzed samples show a <Zn-O>bond distance of 1.978 Å in perfect agreement with the findings of Sowa and Ahsbahs.[35] Moreover, the Δ polyhedral distortion (× 10^4) (as defined by Brown and Shannon)[42] is always lower or equal to 0.09, thus confirming the substantial regularity of the ZnO_4 tetrahedron.

However, NR2L, NR2S, NP and reference sample SA06 show the Zn-O × 3 bond distances, lying in the *xy* plane, shorter (<Zn-O × 3> = 1.9753(8) Å) than the remaining one (<Zn-O> = 1.986(3) Å), which is aligned along the *z* direction. Instead, MR is characterized by an almost perfectly regular tetrahedron. Besides, MR has a displacement parameter of the O site smaller than that of the Zn site, whereas all the remaining samples show comparable values for both sites. Finally, MR is characterized by cell parameters that are significantly larger than those of the other samples.

Following the finding of Kaurova et al.[43], we investigated the possible symmetry reduction from $P6_3/mc$, which is typical of stoichiometric zincite, to $P3$, which has been observed in O-defective zincite. However, no Bragg reflection at ca. 17.2° 2θ, attributed by those authors to the symmetry-violating 001 peak, was observed in all analyzed samples indicating that the correct space group for the present nano-structured zincites is $P6_3/mc$. According to Kaurova et al.[43], the occurrence of O-vacancies is coupled to a marked reduction of the cell parameters, which is not observed in the present samples. Analysis of the micro structural parameters indicates that ε_0 micro-strain (lattice strain), defined as $\beta_i = 4\varepsilon_0 \tan\theta$, β_I being the peak integral breadth[44], takes the larger value of 0.0660(7) in the case of NP. The same sample has a nearly spherical coherency domain ellipsoid of ca. 60 nm in diameter in excellent agreement with the average grain size of 66(20) nm determined from FE-SEM. Differently, the remaining samples are characterized by a marked asymmetry of the principal radii of the coherency domain ellipsoid that shows r_c/r_a ratios ranging from 1.75(2) and 2.05(3).

The coherency domains along the *a*-axis calculated for ZnO-NRs produced by SS and LS and for ZnO-MRs are consistent with their diameters as observed by FE-SEM, whereas the ones estimated along the *c*-axis are significantly shorter than the ZnO-NRs and MRs lengths. Such apparent discrepancy may be justified by polycrystallinity, as it seems to be confirmed by the observation that the principal radii of ZnO-NRs (obtained by LS and SS) are virtually unchanged, indicating that sonication has probably acted as a disaggregation medium.

Table 3. Cell parameters *a*, *c*, *a*/*c*, volume, bond distances and tetrahedral distortion (Δ × 10^4) of the analysed ZnO samples. Reference data SA06[33] from single-crystal analysis are reported for comparison purposes.

	MR	NR2L	NR2S	NP	SA06
***a* (Å)**	3.25110(2)	3.24979(2)	3.24989(2)	3.24987(2)	3.2494(2)
***c* (Å)**	5.20831(4)	5.20637(4)	5.20653(4)	5.20694(5)	5.2054(2)
c/a	1.6020	1.6021	1.6021	1.6022	1.6020
volume (Å^3)	47.6748(7)	47.6186(7)	47.6231(6)	47.6261(8)	47.598(7)
Zn B_{iso}(Å^2)	0.506(9)	0.488(8)	0.493(8)	0.493(8)	*0.52(3)
O B_{iso}(Å^2)	0.35(4)	0.47(4)	0.50(4)	0.40(3)	*0.58(15)
Zn-O x 3 (Å)	1.9792(7)	1.9762(6)	1.9752(6)	1.9745(6)	1.974
Zn-O (Å)	1.977(2)	1.983(2)	1.986(2)	1.988(2)	1.988
<Zn-O>	1.978	1.978	1.978	1.978	1.978
Δ	0.01	0.02	0.06	0.09	0.09

TEM analysis was performed on the samples produced by SS and LS of the paper P2 in acetone. Figure 6A and 6B shows high resolution-TEM (HR-TEM) images of the synthesized ZnO-NRs produced by SS (NR2S) or by LS (NR2L), respectively. The micrographs demonstrate that the nanorods are perfectly crystalline and oriented along the [100] direction, as clearly indicated by the FFT (in the inset). The structure of the NR2L sample, even if perfectly crystalline, appears slightly more damaged, in particular over the surface. Furthermore, images of Z-contrast High Angle Annular Dark Field (HAADF) Scanning Transmission Electron Microscopy (STEM) of the ZnO-NR produced by SS and LS are reported in the SI (Figs. S4 and S5), together with the results of Energy Dispersive X-Ray (EDX) spectroscopy. The HAADF-STEM and EDX analyses revealed that Zn and O are the only elements present in the crystalline structure. The observed composition is unifom with stoichiometry close to ZnO.

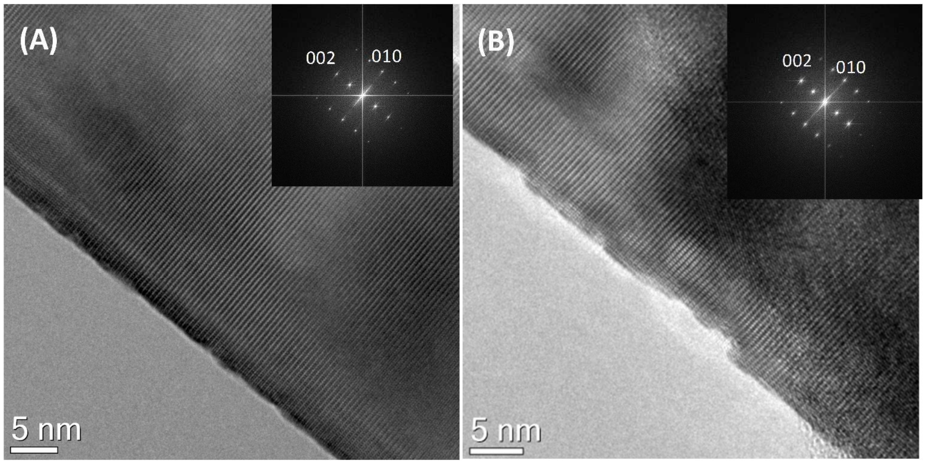

Figure 6. HR-TEM images of the ZnO NR produced from paper P2 by (a) SS and (b) LS samples. The crystal are oriented along the [100] direction as clearly indicated by the FFT (in the inset).

The surface chemical compositions of the ZnO-NRs obtained by LS and SS have been analyzed by XPS in order to detect any trace of impurities and to assess the homogeneity of sample composition. The obtained data are compared with the ones of ZnO-MRs and ZnO-NPs (synthesized according to the procedure described in the SI). In all the samples, zinc is present in the form of ZnO, i.e. in

Zn(+2) chemical state, which is evident from the binding energy (BE) value of Zn $2p_{3/2}$ peak at BE ≈ 1021.3 eV and from the Auger Zn LMM peak position at kinetic energy KE ≈ 988.3 Ev[45,46]. In addition, the value of the modified Auger parameter α ≈ 2010.5 eV corresponds to the Zn(+2) chemical state.[45,47] The spectra of Zn 2p and Zn LMM regions are shown in Figs. 7A and 7B, respectively. The O1s spectra of all the ZnO-NRs samples consists of two components indicated as O1s A and O1s B. The first component is attributed to O_2^- ions in the wurtzite structure of ZnO,[44] while the second one is attributed to the loosely bound oxygen on the surface, such as in adsorbed hydroxyl groups –OH and/or $-CO_3$ radicals.[45,48] The O1s spectra of the ZnO-NRs samples including the peak fitting are presented in Fig. 8A and 8B. The C 1s spectra are similar for both samples and indicate the presence of the aliphatic carbon (component C1s A) and carbonates (C1s B). For better understanding of the differences between the samples, the ratio of Zn and O was computed for the component of oxide O 1s A. In the case of Zn/O > 1, the amount of O is lower in comparison with stoichiometric oxide. In this situation, the lack of oxygen is an indicator of the higher number of defects in zinc oxide. The Zn/O ratios were computed for ZnO-NRs, ZnO-MRs, and ZnO-NPs. The obtained results demonstrated that MRs have the highest number of defects and the NRs obtained by SS have a much lower one. The occurrence of a more extended defectivity agrees with the reported significantly larger cell parameters of MR as compared to the remaining samples. For the different types of ZnO micro/nanostructures it results: for MR Zn/O ratio equal to1.35; for NR2L, it is 1.3; for NPs, it is 1.2; for NR2S, the Zn/O ratio is 1. These results indicate that our preparation method ensured the production of pure oxide in all four nanostructures of ZnO products, as the Zn and O were the only elements detected on the surface. Furthermore, the obtained spectra revealed that LS induces the presence of surface oxygen defects in ZnO-NRs.

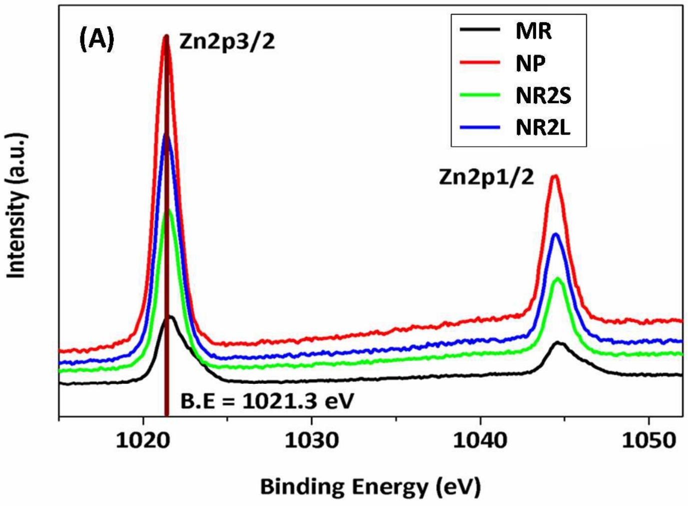

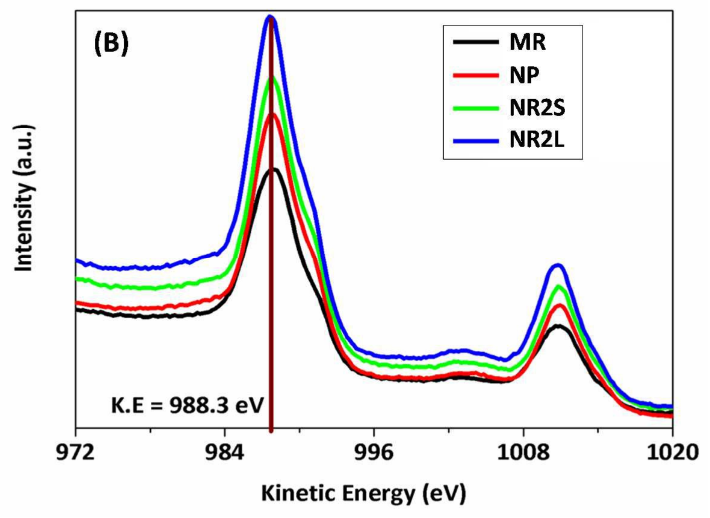

Figure 7. Zn2p spectra (A) and Auger Zn LMM spectra (B) of ZnO-NRs produced from paper P2 by SS and LS, and of ZnO-MRs and ZnO-NPs synthesized as described in the SI.

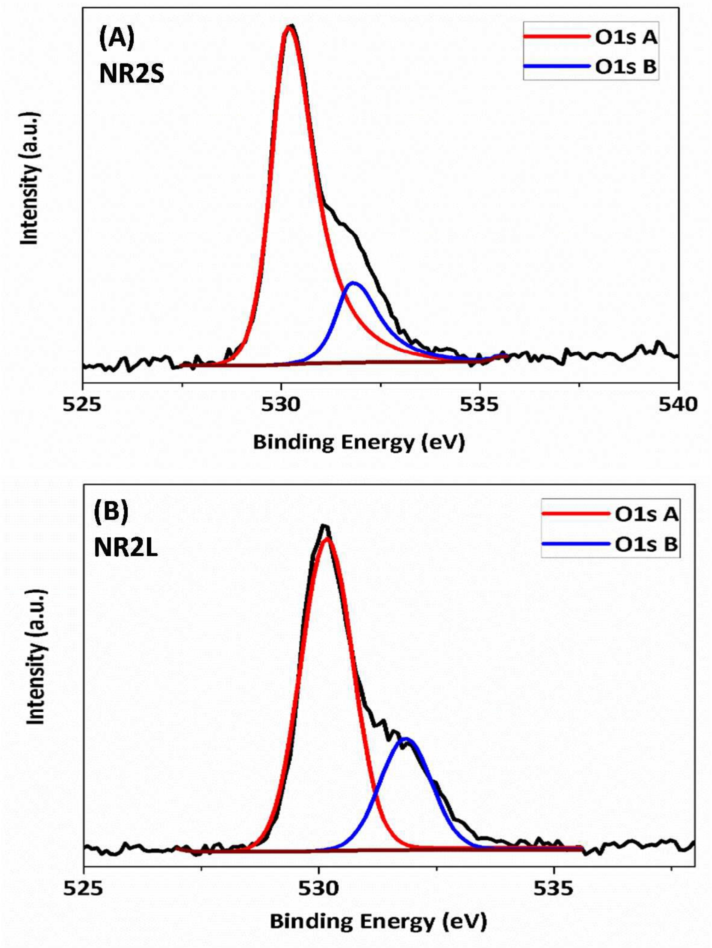

Figure 8. O 1s spectra of ZnO-NRs produced from paper P2 by SS (A) and LS (B).

Photoluminescence spectra of the ZnO-NRs produced with SS and LS have been registered at room temperature and compared to those of MRs and NPs in order to investigate the presence of defects. As it's well known, defects in semiconductor materials will induce energy levels in their band gaps, causing the quenching of direct band edge (BE) emission and, eventually, activating PL bands at lower emission energy.

In ZnO nanostructures, BE emission is typically observed as a sharp ultraviolet (UV) peak at ~ 3.3 eV (380 nm)[49,50]. In addition, different kinds of defects, such as oxygen vacancies, interstitial oxygen, zinc vacancies and interstitial zinc have been reported to contribute to various visible (VIS) bands in the 470-630 nm range of PL spectra of ZnO nanocrystals[51-54]. In particular, for ZnO nanorods it has been also proposed that the visible band around ~ 2.1 eV originates from defects localized near the outmost surface of the nanostructures, within a region of few tens of nanometers[55]. It is also quite intuitive and accepted that structural defects may segregate at surface and grain boundary sites, due to the small dimension of the nanocrystals.

In general, the ratio between UV and VIS PL peak intensity is taken as an indicator of defects concentration of ZnO nanostructures[54,56,57]. This is true as long as the pumping rate does not exceed the surface-recombination rate, i.e., a high enough pumping rate may still produce band-to-band recombination because the surface states are only capable of recombining a limited number of carriers at a given time. For this reason, PL measurements on our samples have been repeated by varying the laser fluence, as reported in SI.

The PL spectra of both ZnO-NRs produced with SS or LS are reported in Fig. 9, they show only a quite intense UV excitonic peak at ~ 3.26 eV and no other emission in all the visible range. The results are obtained for 1300 W/m2 and are in line with those at lower power levels (described in SI). Differently, for the ZnO-MRs, the PL spectrum is dominated by a strong broad visible band with maximum emission at ~2.13 eV, while the very weak band gap emission at ~3.26 eV is hardly detectable at the higher laser power levels and it is completely quenched at 700 W/m^2.

Peak intensities of UV and VIS emissions have been summarized in Table 4 for all samples and laser power levels. The results indicate that defect concentration is lower in both LS and SS NRs, because their UV peak intensity is higher and their VIS/UV ratios lower than the corresponding ones of NPs and MRs. Furthermore, it is noted that UV peak intensity is similar, within the experimental error, for NRs produced by LS and SS. This result is consistent with XRD analysis, showing that the principal radii of ZnO-NRs are virtually unchanged by LS or SS treatment and suggesting that sonication probably acted as a disaggregation medium of the polycrystalline NRs. This consideration is not in contradiction to the TEM and XPS results, indicating that LS induces the presence of surface oxygen defects in ZnO-NRs. In fact, XPS and PL analysis may reveals different kinds of defects: XPS is sensitive to the oxygen vacancies located at the outmost surface of nanostructures, while PL may be affected also by defects occurring at grain boundaries, even if they are embedded inside the nanostructure.

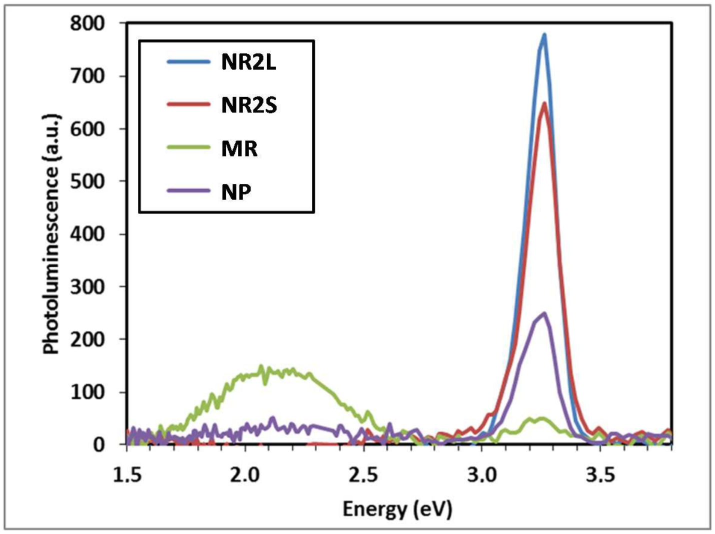

Figure 9. Photoluminescence spectra of of ZnO-NRs produced from paper P2 by SS and LS, and of ZnO-MRs and ZnO-NPs synthesized as described in the SI; incident laser power = 1300 W/m^2.

Table 4. Peak intensities of UV and VIS emissions of the produced material samples (i.e. MR, NP, NR2L and NR2S) for increasing laser power intensity.

Sample	Power (W/m2)	UV PL Intensity (a.u.)	VIS PL Intensity (a.u.)
MR	700 ±100	0±10	90±10
	900 ±100	28±9	100±10
	1300 ±100	50±8	140±10
NP	700 ±100	50±8	-
	900 ±100	110±10	-
	1300 ±100	250±10	20±10
NR2L	700 ±100	110±10	-
	900 ±100	350±20	-
	1300 ±100	780±60	-
NR2S	700 ±100	80±10	-
	900 ±100	250±10	-
	1300 ±100	650±30	-

Conclusions

In the present work, we proposed a synthesis route based on the thermal decomposition method, for mass-production of high-purity ZnO-NRs with controlled morphology, uniform diameter, and single-mode length distribution. The proposed approach combines thermal decomposition of zinc acetate dihydrate with probe sonication in acetone.

A multi-technique characterization of the produced nanostructures is approached in order to validate the proposed synthesis route, through the assessment of ZnO structural and physical properties.

The optimum precursor amount of 0.3 g for the growth time of 12 h at 300°C allows the production of ZnO-NRs with high purity, but dual-mode distribution of the nanostructure lengths. We demonstrated that probe sonication in pulsed mode of the synthesized ZnO-NR porous materials dispersed in acetone, for 20 min with ultrasound amplitude of 70%, does not affect the diameter, purity and photoluminescence properties of the 1D nanostructures, but it enables to obtain ZnO-NR powders with single-mode distribution of lengths, with average value of ~470 nm.

The PL spectra of the produced ZnO-NRs indicate the excellent quality of the nanostructures, since their UV emission is much higher than that detected in ZnO-MRs and ZnO-NPs samples and no visible emission is observable in the entire investigated energy range (down to 1.4 eV) and laser power levels (700-1300 W/m^2).

We can conclude that the proposed production route of ZnO-NRs characterized by uniform size distribution is suitable for large-scale applications. The possibility to control the ZnO-NR morphology, combined with a cost-effective synthesis route, enabling mass production and guaranteeing high quality, makes these nanostructures suitable for use as filler in polymeric matrix for the development of new piezoresistive and piezoelectric materials.

Acknowledgements

We are thankful to Dr. Vittorio Morandi and Dr. Andrea Migliori (CNR-IMM Section of Bologna, Italy) for performing TEM analyses, HR-TEM imaging, HAADF-STEM and EDX spectroscopy, and for their helpful comments and discussion.

References:

1. Sheng Xu and Zhong Lin Wang, *Nano Res*, 2011, **4**, 1013.
2. Wang, Z. L. and Wu, W., *Angew. Chem.* Int. Ed., 2012, **51**, 11700.
3. Ae Jung Huh and Young Jik Kwon, *J. Controlled Release*, 2011, **156**, 128.
4. Klingshirn, C., *ChemPhysChem*, 2007, **8,** 782.
5. Y. Zhang, Manoj K. Ram, Elias K. Stefanakos, and D. Y. Goswami, *J. Nanomaterials,* 2012, **2012**, (Article ID 624520).
6. Dazhi Sun, Nobuo Miyatake and Hung-Jue Sue, *Nanotechnology*, 2007, **18**, 215606.
7. Ozgur. U, Daniel Hofstetter, and Hadis Morkoc, *Proceedings of the IEEE,* 2010, **98**, 1255.
8. Q. Zhang, Christopher S. D., X. Zhou, and Guozhong Cao, *Adv. Mater*. 2009, **21**, 4087.
9. Paula Judith Perez Espitia, Nilda de Fátima Ferreira Soares, Jane Sélia dos Reis Coimbra, Nélio José de Andrade, Renato Souza Cruz, Eber Antonio and Alves Medeiros, *Food and Bioprocess Technology,* 2012, **5**, 1447-1464.
10. Bekermann D. et al, *ChemPhysChem,* 2010, 11, 2337 – 2340
11. Barreca D., et al., *Sensors and Actuators B*, 2010, 149, 1–7.
12. Gyu-Chul Yi, Chunrui Wang, and Won Il Park, *Semiconductor Science and Technology*, 2005, **20**, pg. S22.
13. Christian Falconi, G. Mantini, Arnaldo D'Amico, and Wang Z. L., *Sensors and Actuators B*, 2009, **139** 511.

14. I. Rago, C. Reddy Chandraiahgari, M.P. Bracciale, G. De Bellis, E. Zanni, M. Cestelli Guidi, D. Sali, A. Broggi, C. Palleschi, M. S. Sarto and D. Uccelletti, *RSC Adv.*, 2014, **4**, 56031.
15. C. Chun Chen, Nan Ye, Chuan Fu YU and Ting FAN, *J. Ceramic Processing Research,* 2014, **15**, 102.
16. Sambhaji S. Warule, Nilima S. Chaudhari, Bharat B. Kale and M. A. More; *CrystEngComm*, 2009, **11**, 2776.
17. Prabhakar Rai, Sudarsan Raj, In-Hwan Lee, Woon-KiKwak and Yeon-Tae Yun, *Ceramics International*, 2013, **39,** 8287.
18. Huang, M. H., Wu, Y., Feick, H., Tran, N., Weber, E. and Yang, P., *Adv. Mater.,* 2001, **13**, 113.
19. Wang Y. W., Zhang L. D., Wang G. Z., Peng X. S., Chu Z. Q. and Liang C. H. *J. Cryst. Growth*, 2002, **234**, 171.
20. Yang, P., Yan, H., Mao, S., Russo, R., Johnson, J., Saykally, R., Morris, N., Pham, J., He, R. and Choi, H.-J., *Adv. Funct. Mater.*, 2002, **12**, 323.
21. Li S. Y., Lee C. Y. and Tseng T. Y., *J. Cryst. Growth*, 2003, **247**, 357.
22. Park W. I., Kim D. H., Jung S. W. and Yi G. C., *Appl. Phys. Lett*., 2002, **80**, 4232.
23. Park W. I., Yi G. C., Kim M. Y. and Pennycook S. J., *Adv. Mater.*, 2002, **14**, 1841.
24. Liu B. and Zeng H. C., *J. Am. Chem. Soc.*, **2003**, ***125***, 4430.
25. Li Z. Q., Xie Y., Xiong Y. J., Zhang R. and He W., *Chem. Lett.*, 2003, **32**, 760.
26. Tian Z. R. R., Voigt J. A., Liu J., Mckenzie B. and Mcdermott M. J., *J. Am. Chem. Soc.*, 2002, **124**, 12954.
27. Vayssieres L., *Adv. Mater*., 2003, **15**, 464.
28. Yin M., Gu Y., Kuskovsky I. L., Andelman T., Zhu Y. M., Neumark G. F. and O'Brien S., *J. Am. Chem. Soc.*, 2004, **126**, 6206.
29. Chih-Cheng Lin, and Yuan-Yao Li, *Material Chemistry and Physics*, 2009, **113,** 334.
30. Chih-Cheng Lin, Wang-Hua Lin and Yuan-Yao Li, *J. Phys. D Appl. Phys.*, 2008, **41**, 225411.
31. Sunandan Baruah and Joydeep Dutta; *Sci. Technol. Adv. Mater.,* 2009, **10**, 013001.
32. D. Polsongkrama, P. Chamninok, S. Pukird, L. Chow, O. Lupan, G. Chai, H. Khallaf, S. Park, and A. Schulte, *Physica B*, 2008, **403**, 3713.
33. S. Hussain, Tianmo Liu, M. Kashif, Liyang Lin, Shufang Wu, Weiwei Guo, Wen Zeng, U. Hashim, *Materials Science in Semiconductor Processing*, 2014, **18**, 52.
34. Sheng Xu, Changshi Lao, Benjamin Weintraub, and Zhong Lin Wang, *J. Mater. Res.,* 2008, **23**, 884.
35. Sowa H., and Ahsbahs H., *Journal of Applied Crystallography*, 2006, **39**, 169.
36. Sabine, T.M., Hunter, B.A., Sabine, W.R., and Ball, C.J., *Journal of Applied Crystallography*, 1998, **31**, 47.
37. Ballirano, P., *Journal of Applied of Crystallography*, 2003, **36**, 1056.
38. Katerinopoulou A., Balic-Zunic T., and Lundegaard L.F., *Journal of Applied Crystallography,* 2012, **45**, 22.
39. Di Marco M., Port M., Couvreur, P., Dubernet C., Ballirano P., and Sadun C., *Journal of the American Chemical Society,* 2006, **128,** 10054.
40. Di Marco M., Ballirano P., Port M., Piscopiello E., Couvreur P., Dubernet C., and Sadun C. *Journal of Materials Chemistry*, 2009, **19**, 6354.
41. Ballirano P., De Vito C., Ferrini V., and Mignardi S., *Journal of Hazardous Materials*, 2010, **178**, 522.

42. Brown, I.D. and Shannon, R.D., *Acta Crystallographica*, 1973, **A29**, 266.
43. Kaurova, I.A., Kuzmicheva, G.M., and Rybakov, V.B., *Crystallography Reports*, 2013, **58**, 226.
44. Ballirano, P. and Sadun, C., *Structural Chemistry*, 2009, **20**, 815.
45. Moulder J. F., Stickle W. F., Sobol P. E., Bomben K. D., *Handbook of X-ray Photoelectron Spectroscopy* (2^{nd} edn), Chastain J (editor). Perkin-Elmer Corp., Physical Electronic Division: Eden Prairie, 1992.
46. Barreca D., Gasparotto A., Maccato C., Maragno C. and Tondello E., *Surf. Sci. Spectra*, 2007, **14**, 19.
47. S. Kaciulis, L. Pandolfi, E. Comini, G. Faglia, M. Ferroni, G. Sberveglieri, S. Kandasamy, M. Shafiei, W. Wlodarski, *Surf. Interface Anal.*, 2008, **40**, 575.
48. S. Kaciulis, G. Mattogno, A. Galdikas, A. Mironas, and A. Setkus, *J. Vac. Sci. Technol.*, 1996, **A14**, 3164.
49. Michael Breeedon, Colin Rix, and Kourosh Kalantar-zadeh, *Materials Letters*, 2009, **63**, 249.
50. M. H. Huang, S. Mao, H. Feick, H. Q. Yan, Y. Y. Wu, H. Kind, E. Weber, R. Russo and P. D. Yang, *Science,* 2001, **292**, 1897.
51. A. B. Djurisic, Y. H. Leung, K. H. Tam, L. Ding, W. K. Ge, H. Y. Chen and S. Gwo, *Appl. Phys. Lett.,* 2006, **88**, 103107.
52. L. Wu, Y. Wu, X. Pan, and F. Kong, *Opt. mater.*, 2006, **28,** 418.
53. Y. Y. Tay, T. T. Tan, M. H. Liang, F. Boey and S. Li, *Phys. Chem. Chem. Phys.*, 2010, **12,** 6008.
54. Shalish, I; Temkin, H; Narayanamurti, V; Physical Review B, 2004, 69, 245401.
55. Shan Jiang, Zhaohui Ren, Siyu Gong, Simin Yin, Yifeng Yu, Xiang Li, Gang Xu, Ge Shen, and Gaorong Han, *Applied Surface Science,* 2014, **289,** 252.
56. L.H. Quang, S. J. Chua, K. P. Loh, and E. Fitzgerald, *J. Cryst. Growth*., 2006, **287,** 157.
57. Teng-Jiao Liu, Qi Wang and Peng Jiang, *RSC Adv*., 2013, **3**, 12662.

Figure Legends:

Figure 1. Schematic of the ZnO-NRs production route and characterization process.

Figure 2. FE-SEM images of ZnO-NRs on the top (A, C, E, G) and bottom (B, D, F, H) faces of the porous paper grown under different conditions: 0.1 g of precursor and 12 h at 300°C (A,B); 0.3 g of precursor and 12 h at 300°C (C,D); 0.5 g of precursor and 12 h at 300°C (E,F); 0.3 g of precursor and 6 h (G,H) at 300°C.

Figure 3. FE-SEM images of ZnO-NRs produced through SS (A, B) or LS (C, D) in acetone of the porous paper grown for 12 h at 300°C using 0.3 g of precursor.

Figure 4. Length CDF of ZnO-NRs produced with 0.3 g of precursor (A) and diameter CDF of the NRs obtained by LS of the paper P2 (B).

Figure 5. X-ray diffraction patterns of ZnO-NRs produced from paper P2 by SS and LS, and of ZnO-MRs and ZnO-NPs synthetized as described in the SI.

Figure 6. HR-TEM images of the ZnO NR produced from paper P2 by (a) SS and (b) LS samples. The crystal are oriented along the [100] direction as clearly indicated by the FFT (in the inset).

Figure 7. Zn2p spectra (A) and Auger Zn LMM spectra (B) of ZnO-NRs produced from paper P2 by SS and LS, and of ZnO-MRs and ZnO-NPs synthesized as described in the SI.

Figure 8. O 1s spectra of ZnO-NRs produced from paper P2 by SS (A) and LS (B).

Figure 9. Photoluminescence spectra of of ZnO-NRs produced from paper P2 by SS and LS, and of ZnO-MRs and ZnO-NPs synthesized as described in the SI; incident laser power = 1300 W/m^2.

Table Legends:

Table 1. ZnO-NR papers produced under different experimental conditions (precursor amount and growth time): measured weight and production yield.

Table 2. Mean values and standard deviations (in brackets) of diameter and length of ZnO-NRs on the top or bottom sides of the papers listed in Table 1, and obtained by LS of the paper P2.

Table 3. Cell parameters *a*, *c*, *a*/*c*, volume, bond distances and tetrahedral distortion ($\Delta \times 10^4$) of the analysed ZnO samples. Reference data SA06[34] from single-crystal analysis are reported for comparison purposes.

Table 4. Peak intensities of UV and VIS emissions of the produced material samples (i.e. MR, NP, NR2L and NR2S) for increasing laser power intensity.